Journal of Instrumentation



**PAPER** • **OPEN ACCESS**

# Interferometry analysis with fringe normalization and matrix Abel inversion for plasma diagnostics

To cite this article: S. Lee *et al* 2023 *JINST* **18** C12016



Published by IOP Publishing for Sissa Medialab

Received: *September 1, 2023*
Accepted: *November 7, 2023*
Published: *December 21, 2023*

20TH International Symposium on Laser-Aided Plasma Diagnostics
Kyoto, Japan
10–14 September 2023

2023 JINST 18 C12016

# Interferometry analysis with fringe normalization and matrix Abel inversion for plasma diagnostics

**S. Lee,**[a] **I. Nam,**[b] **M. Cho,**[b] **D. Jang,**[b] **S. Kwon,**[b] **H. Suk**[a,*] **and M. Kim**[b,*]

[a] *Department of Physics and Photon Science, Gwangju Institute of Science and Technology, Gwangju 61005, Republic of Korea*
[b] *Pohang Accelerator Laboratory, POSTECH, Pohang 37673, Republic of Korea*

*E-mail:* hysuk@gist.ac.kr, kms83@postech.ac.kr

Abstract: In plasma diagnostics using interferometry, the phase shift caused by the plasma in the fringes is extracted to determine the plasma density. The common method to extract the phase shift from the fringes is the fast-Fourier-Transform (FFT), but this technique encounters challenges when dealing with insufficient fringe numbers, spatially varying fringe frequencies, or extremely sharp phase changes. These challenges result in errors and hinder the acquisition of precise phase measurements. To tackle this issue, we introduced the fringe normalization (FN) method. The simulations demonstrated that the FN method extracts accurate phase information, surpassing the capabilities of the FFT method. As a result, this advancement enables more precise plasma diagnostics by mitigating errors that arise during the phase data processing. Furthermore, we improved the code for the inverse matrix Abel inversion to convert phase information into density. The simulation employing this code showed that the developed code provides more accurate values in the analysis of plasmas with a sharp density profile, assisting in electron beam manipulation in laser-plasma acceleration.

Keywords: Plasma diagnostics - interferometry, spectroscopy and imaging; Wake-field acceleration (laser-driven, electron-driven)

*Corresponding author.



https://doi.org/10.1088/1748-0221/18/12/C12016

## Contents



## 1 Introduction

Plasma diagnostics represent a crucial method for its efficient application in plasma-based researches. Plasma characteristics such as temperature and density have been analyzed using a range of methods including spectroscopy and interferometry [1–3]. One of typical techniques for plasma density measurement is optical laser interferometry, which entails the analysis of phase shift induced by plasma in interference fringes. Because the phase shift is proportional to the electron number density in the interferometry scheme, the accurate analysis of phase information is a critical process. Such analysis has primarily been conducted using a fast-Fourier-transform (FFT) method [4]. However, under constrained conditions that involve abrupt plasma density variations or yield a limited number of fringes, errors can arise during data processing.

In laser wakefield acceleration (LWFA) researches, the plasma profile with a sharp density transition plays a crucial role in the injection and acceleration of electrons [5–7]. Narrow and high density distribution may be used for short injection resulting in a narrow spectrum and high charge electron beams, and long or inclined density profile can be used for longer acceleration length. Therefore, precise measurement of steep plasma density gradients is essential for effective electron beam control in LWFA applications.

In this study, we introduced the fringe normalization (FN) method to reduce an error in phase analysis. The FN is an algorithm to extract the phase information from single fringe pattern with non-uniform amplitude [8, 9], and from comparative simulation with the FFT method, we confirmed that the FN method enhances the accuracy in phase analysis under some constrained conditions. Furthermore, we improved the inverse matrix Abel inversion method [10, 11] as a means of converting phase shift to density function. To check validity of proposed methods, we conducted simulations for plasma density analysis by assuming defined density profile which can be used in LWFA.



2023 JINST 18 C12016

## 2 Fringe normalization method

### 2.1 Fringe normalization

The purpose of FN is to map appropriately the data values within the range of −1 to 1, facilitating the effective utilization of the inverse cosine function. To apply FN, let's assume that the fringe data, the intensity $I(x)$ of the signal, are represented as

$$I(x) = A(x) \cdot \cos(\phi(x)) + DC(x). \tag{2.1}$$

To obtain the normalized fringe signalcos$(\phi(x))$, we employ the most intuitive peak-based method, then $DC(x)$ and $A(x)$ are extracted from $I(x)$.

The first step for $C(x)$ is setting *upper peaks* and *lower peaks* of $I(x)$ (figure 1a). After interpolating the *upper peaks*, an envelope of upper part ($env_+$) is obtained. Similarly, the obtained *lower peaks* give the lower envelope ($f_-$). Here we define $DC_1(x)$ as an average of $env_+$ and $env_-$. By subtracting $DC_1(x)$ from $I(x)$ we define $I_1(x)$, and similar process of finding new $env_+$ and $env_-$ is repeated by finding $DC_2(x)$ and $I_2(x)$, and so on.

$$\begin{aligned} I_2(x) = I_1(x) &= A(x)\cos(\phi(x)) + DC(x) - DC_1(x) \\ I_3(x) &= I_2(x) - DC_2(x), \ldots \end{aligned} \tag{2.2}$$

After $n$ steps $DC_n(x)$, it will converge to zero at large $n$. Then, $DC(x)$ can be expressed as the sum of $DC_k(x)$: $DC(x) = \sum_{k=1}^{n} DC_k(x)$. However, blindly increasing $n$ can actually lead to more errors between $DC(x)$ and $\sum_{k=1}^{n} DC_k(x)$. The reason is that there are numerical errors during interpolation when using *peaks*. Here, we propose the linear interpolation and opt up to $n = 2$ in the data process. Now, we obtain a new signal ($I_{\text{amp}}(x)$) after removing $DC(x)$: $I_{\text{amp}}(x) = I(x) - DC(x)$.

Next, we remove the amplitude function $A(x)$. If the $DC(x)$ is effectively eliminated in the above process, the upper and lower sides of the envelope of $I_{\text{amp}}(x)$ should be balanced around the center zero. To make more peaks we add $-I_{\text{amp}}(x)$ to $I_{\text{amp}}(x)$ and pick up the *upper peaks*, which will give $A(x)$. The red line in figure 1b shows after the interpolation. There can be some points of $I_{\text{amp}}(x)$ that are larger than $A(x)$, especially where $A(x)$ significantly variate. This issue would be resolved by changing the interpolation method or adjusting the positions of the peaks. However, the simplest solution is to set those points forcing the same values $A(x)$ to $I_{\text{amp}}(x)$. When all points satisfy $A(x) \geq |I_{\text{amp}}(x)|$, then we can get the normalized fringe $I_{\text{norm}}(x)$ (figure 1c) by dividing $A(x)$: $I_{\text{norm}} = I_{\text{amp}}(x)/A(x)$.

There are two more issues to be cautious when processing the original data. The first is to accurately identify positions of peaks, i.e., correctly captured points where the phase ($\phi(x)$) should become an integer of $\pi$. The second is to avoid data before the first peak and after the last peak since it cannot be obtained through the interpolation.

### 2.2 Phase retrieving with inverse cosine function

The obtained $I_{\text{norm}}(x)$ will have $\cos(\phi(x))$ like eq. (2.1), so the phases are obtained by $\phi_{\text{arc}}(x) = \text{acos}(I_{\text{norm}}(x))$. Since the inverse cosine function ranges $[0, \pi]$, it is necessary to map appropriately the values in the range of $[0, 2\pi]$ to align with the periodicity of the cosine function. When the phase $\phi(x)$ is appropriately mapped within the range of $[0, 2\pi]$: $\phi_{\text{wrap}}$, it satisfies the following



2023 JINST 18 C12016

equation: $\phi(x) = \phi_{\text{wrap}}(x) + 2\pi N$ ($N$ is an integer). We can determine $\phi_{\text{wrap}}$ considering the $\phi_{\text{arc}}$ slope:

$$\phi_{\text{wrap}}(x) = \begin{cases} \phi_{\text{arc}}(x): & \left(\phi'_{\text{arc}}(x) \geq 0\right) \\ 2\pi - \phi_{\text{arc}}(x): & \left(\phi'_{\text{arc}}(x) < 0\right) \end{cases}, \tag{2.3}$$

where $\phi'_{\text{arc}}(x)$ is the derivative of $\phi_{\text{arc}}(x)$. There are *peaks* where the sign of $\phi'_{\text{arc}}(x)$ is not determined due to the discontinuity as shown in figure 2a. In such peaks, we choose the smaller slope of $\phi_{\text{wrap}} - \phi_{\text{arc}}$ or and $\phi_{\text{wrap}} - [\phi_{\text{arc}} - (2\pi - \phi_{\text{arc}})]$ into $\phi_{\text{wrap}}$ connecting to neighbor points. Afterward, by unwrapping $\phi_{\text{wrap}}$ to ensure the function is continuously connected, $\phi(x)$ is obtained finally (figure 2b).

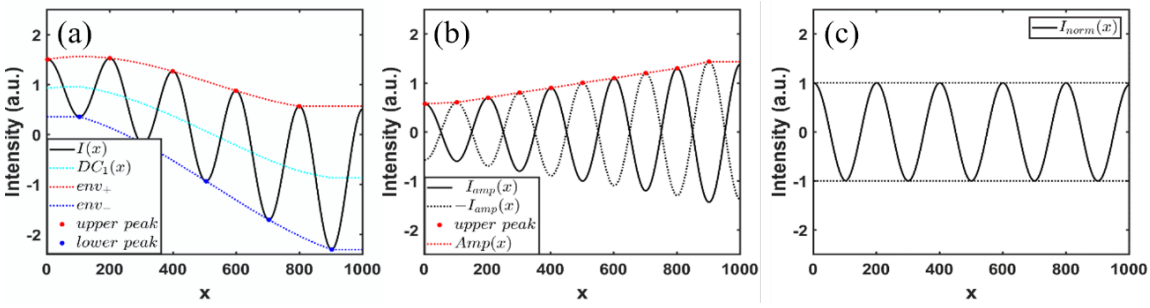


**Figure 1**. (a) shows the intensity $I(x)$ of an arbitrary test signal along with its *upper peak* and *lower peak*, which were used to obtain their respective envelopes, $env_+$ and $env_-$. Additionally, it displays the average of these two envelopes, $DC_1(x)$. (b) shows $I_{\text{amp}}(x)$, obtained by removing $DC_1(x)$ from $I(x)$, along with its graph $-I_{\text{amp}}(x)$ flipped with respect to zero. It presents the envelope $Amp(x)$ derived from the upper peaks of these two curves. (c) shows the normalized intenstiy($I_{\text{norm}}(x)$).

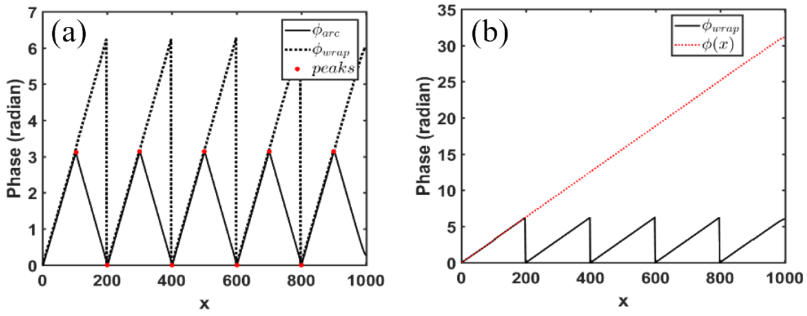


**Figure 2**. (a) The graph of $\phi_{\text{arc}}(x)$ obtained using the acos function and the graph of $\phi_{\text{mod}}(x)$ obtained by extending it to the range of $[0, 2\pi]$. The peaks marked with red dots should be handled with caution when extending the range. (b) shows $\phi_{\text{mod}}(x)$ and its unwrapped version $\phi(x)$.

### 2.3 Phase shift calibration

Phase shift is defined as difference between the signal phase and reference (or carrier) phase. When there are no images of the reference signal available, we can select a portion of the image where no phase shift occurs. Of course, this phase-shift-free portion should be strategically positioned to avoid passing through a plasma or gas before conducting interferometry measurements. We choose the part



2023 JINST 18 C12016

without phase shift and apply the least square method for one-dimensional fitting. The resulting fitting can then serve as a reference phase. If noise signals are low, first-order interpolation would suffice. However, in cases where the frequency of carrier fringe varies across space, higher-order fitting might become necessary. An experimental result is shown in figure 3. In figure 3a, the measured interference pattern passing through a plasma is depicted, while figure 3b showcases the outcomes of the phase shift using the FN method. The latter reveals a distinct plasma density formation.

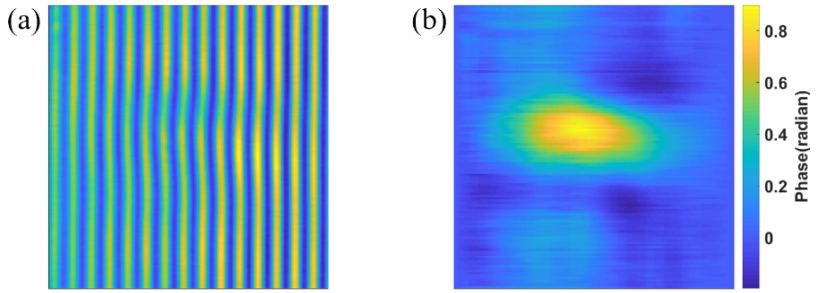


**Figure 3**. (a) shows the interference fringes with laser induced plasma. (b) shows retrieved phase shift of (a) by using FN method.

### 2.4 Comparison of FN and FFT methods

In this section, we will compare the simulation results of the FFT method and the FN method using different numbers of fringes with MATLAB. To conduct the simulation, we first determine the size of the domain and create a reference signal with no phase shift (represented by the red dotted line in figure 4a), aligned with the number of fringes to be used. Then we added an arbitrary phase shift (represented by the black line in figure 4b) to create a modulated signal (represented by the black line in figure 4a). We analyzed these signals separately using the FFT method and the FN method, comparing the phase shift value obtained with the phase shift values introduced during signal modulation to confirm the errors that occurred depending on the method used. In this simulation, we assumed that there is no noise in the signal itself, and that the amplitude change is also smooth, in order to discuss the effectiveness of the method itself.

In figure 4b, a comparison is presented between the original phase shift, the phase shift retrieved through the FFT method, and that retrieved via the FN method. Figures 4c–f display the phase errors at fringe numbers 15, 20, 25, and 30, respectively. As the number of fringes increases, the phase errors decrease when using the FFT method. On the other hand, the FN method exhibits quite small errors even with just 15 fringes, and these errors further diminish as the number of fringes increases. Ultimately, the FN method provides more accurate results compared to the FFT method.

The challenge when applying the FN method to real data is whether it can accurately capture the correct envelope points or not. However, this is not a problem with the FN methodology but rather a question of whether noise handling and peak detection can be performed accurately. Fortunately, the FN method allows for easy correction of error points by directly identifying them. Another issue could arise when intensity changes between fringes are not linear. However, if this fact is known, one can use high-order approximations tailored to it.



2023 JINST 18 C12016

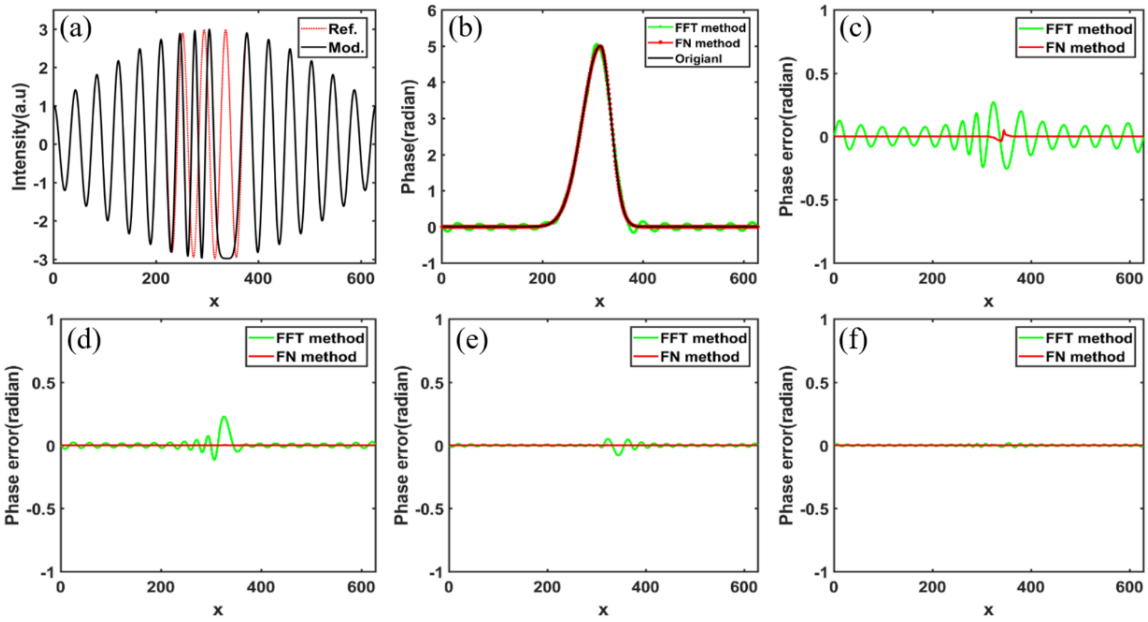


**Figure 4**. (a) shows modulated fringe data. (b) shows phase shift added to the reference signal. (c), (d), (e) and (f) plots represent the errors in the phase variation obtained using the FFT and FN methods for fringe counts of 15, 20, 25, and 30, respectively.

## 3 Inverse matrix Abel inversion

The Abel inversion is a mathematical technique that allows us to reconstruct the internal density function using its projection image. It assumes that the internal density function, denoted as $f(r)$, is a function of the radial variable. Given a projection image $I(x)$, the density function $f(r)$ can be expressed as follows:

$$f(r) = -\frac{1}{\pi}\int_r^\infty \frac{dF}{dx}\frac{dx}{\sqrt{x^2 - r^2}}\,. \tag{3.1}$$

When directly applying eq. (3.1), errors due to discretization can significantly impact the reconstructed density function. After discretizing values of $I_i$ and $f_j(i, j = 1, \ldots, N)$, they can be expressed using matrix notation as follows:

$$\begin{bmatrix} M_{1,1} & \ldots & M_{1,N} \\ \ldots & M_{i,j} & \ldots \\ M_{N,1} & \ldots & M_{N,N} \end{bmatrix} \begin{bmatrix} f_1 \\ \ldots \\ f_N \end{bmatrix} = \begin{bmatrix} I_N \\ \ldots \\ I_N \end{bmatrix}, \tag{3.2}$$

where $M$ is $N \times N$ matrix that depends on the specific transformation. Assuming $I(x)$ represents a projection of a radial density function, $M$ becomes upper triangular matrix and invertible, this allow us to calculate the density function $f$ using the equation $f = M^{-1} \times I$. To determine the matrix $M$, let's assume a semicircle with a radius of $N$. We assume that its density function takes the form $\rho(r(x, y)) = N - \sqrt{r^2}$, where $r^2(x, y) = (x - 1)^2 + (y - 1)^2$. Then, we can make the $M_{ij}$ by counting the number of $y$ that satisfy the following condition:

$$M_{ij} = \text{count}\{y | N - j + 1 < \rho(r(i, y)) \leq N - j + 2 : y \text{ is an integer}\}.$$



2023 JINST 18 C12016

Figure 5a illustrates the computed matrix $M$ with $N = 100$. As the size of matrix $M$ increases, the values of $f_j$ become more accurate. Therefore, the projection $I(x)$ is discretized using a larger number of points. We only need to consider $f_j$ values that correspond to the measured $I(x)$ as $f(r)$. In figure 5b, a comparison is made among the original density function, the density function retrieved using the inverse matrix method, and the density function directly calculated using eq. (3.2). The inverse matrix method yields a more accurate result at $N = 1000$ compared to $N = 100$. However, significant errors are observed in the first grid value $f_1$. Hence, for now, it is recommended to extrapolate $f_1$ from the values of $f_{2\sim N}$ rather than using the directly obtained value.

When applying this to real data, there are several points to be considered. Firstly, it's about determining the center position of the plasma. Finding the center of a plasma that exhibits left-right symmetry is essential, but since real data is often asymmetric, the choice of what to consider as the center can significantly affect the results. We plan to develop code that utilizes the inverse matrix method for asymmetric Abel inversion to address this issue. Next, there is issue of dealing with problems that arise at the plasma's boundary. As the laser passes through the plasma's outer region, it undergoes refraction, leading to additional phase changes and causing ambiguity in precisely determining the boundary. The effects of refraction not only impact the phase but also affect the intensity, so we plan to improve the code by incorporating a method that considers intensity in defining the boundary.

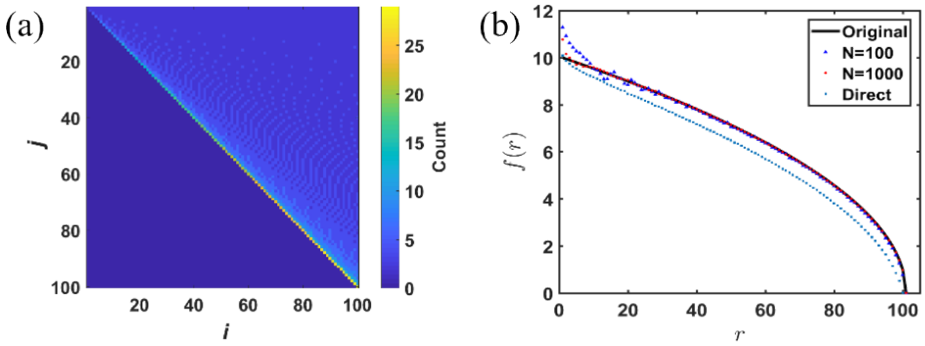


**Figure 5**. (a) shows the $M$ with $N = 100$. (b) shows the original denstiy function with reconstructed density function by inverse matrix method (N=100 and 1000) and direct method.

## 4 Simulation for plasma density analysis

There exists a relationship between the plasma density ($n_e$) and the differential phase ($d\phi$), which can be expressed as follows [12]:

$$d\phi = \frac{e^2}{-2c^2 k_0 \epsilon_0 m_e} n_e dx\,, \tag{4.1}$$

where $k_0$ is the wavenumber of the probe laser and $dx$ is the differential length of plasma. The phase shift ($\Delta\phi = \int d\phi$) is obtained by the FN method. This phase shift is then utilized in the Abel inversion process to estimate the electron density of $n_e$.

For density analysis calculations, a signal was tested under following conditions. The maximum plasma density at the center is $5 \times 10^{24}\,\mathrm{m}^{-3}$, with a cross-section profile following a one-sigma



2023 JINST 18 C12016

Gaussian shape of 0.2 mm (represented by the black line in figure 6d). The longitudinal electron density profile is shown as a black solid line in figure 6c. The corresponding phase shift is presented in figure 6b. In order to validate our algorithm, we introduce the phase shift to the reference data with 20 fringes, and the generated signal data is shown in figure 6a, and reconstructing the data is shown in figure 6e. As demonstrated in figure 6c, there is a noticeable agreement with the original one. In figure 6d, after dividing into 20 segments using the inverse matrix method, the value $f_1$ obtained by the spline interpolation was slightly lower at the center axis, measuring 0.947 compared to the original value of 1.0. The final calculated electron density amount to $4.73 \times 10^{24}$ m$^{-3}$, whereas the original value stood at $5.0 \times 10^{24}$ m$^{-3}$.

In the actual plasma where LWFA phenomena occur, the phase changes are often too subtle to be directly observed. Therefore, it is necessary to artificially extend the length of the plasma for measurements. It appears that further research is needed to understand how the process of increasing the size of the plasma at the same gas density nonlinearly affects the plasma density.

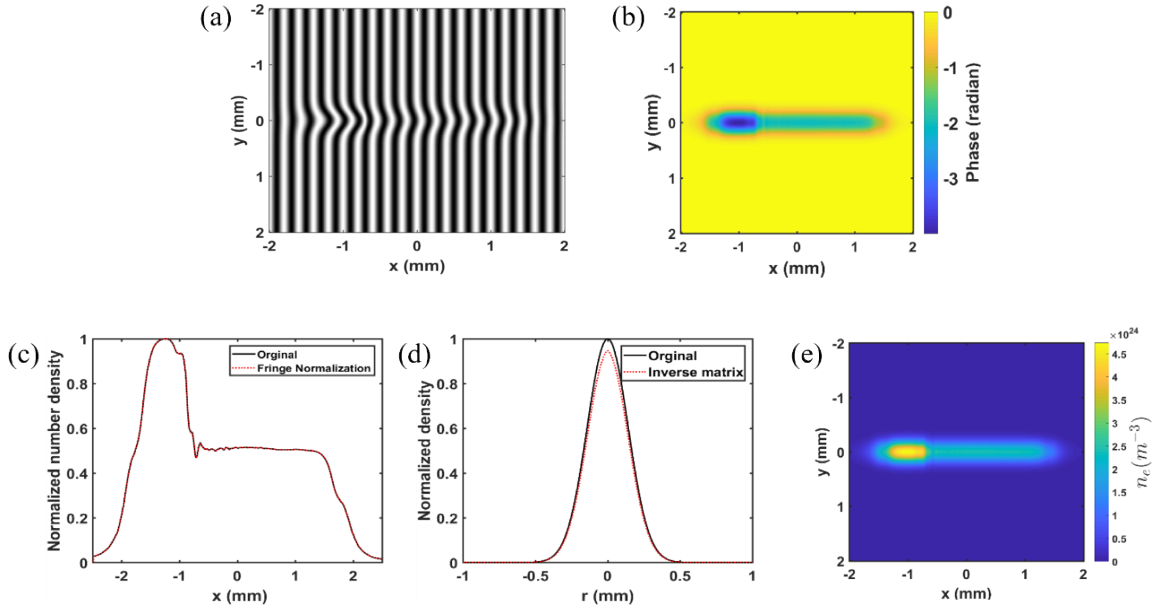


**Figure 6**. (a) The generated fringe data. (b) The generated phase shift map. (c) Normalized density distribution along the x-axis. (d) Normalized density distribution of cross-section. (e) Retrieved electron number density map.

## 5 Conclusion

We introduced two data processing algorithms of the FN method and inverse matrix Abel inversion to diagnose a plasma density with the laser interferometry. The FN method could show more accuracy than the FFT method. The inverse matrix Abel inversion, as finding better matrix M, it could work effectively even at a small size. Our data process promised capability in plasma density diagnostics through a virtual plasma test with its accurate and efficient data analysis. The next goal will be to demonstrate that this analysis method works properly using real experimental data in the future. Further research and exploration of these algorithms could lead to significant advancements in the laser interferometry applications for plasma diagnostics, especially in LWFA.



2023 JINST 18 C12016

## Acknowledgments

This work was supported by the National Research Foundation of Korea (NRF) funded by the Korea government (MSIT) [No. 2020R1C1C1011840, 2020R1C1C1010477, 2021R1C1C1003255, 2021R1F1A1062911, 2022R1A2C2009768, 2022R1A2C3013359]

## References

[1] A.J. Gonsalves et al., *Transverse Interferometry of a Hydrogen-Filled Capillary Discharge Waveguide*, *Phys. Rev. Lett.* **98** (2007) 025002.

[2] D.G. Jang et al., *Density evolution measurement of hydrogen plasma in capillary discharge by spectroscopy and interferometry methods*, *Appl. Phys. Lett.* **99** (2011) 141502.

[3] M.S. Kim et al., *Characteristics of a tapered capillary plasma waveguide for laser wakefield acceleration*, *Appl. Phys. Lett.* **102** (2013) 204103.

[4] M. Takeda, H. Ina and S. Kobayashi, *Fourier-transform method of fringe-pattern analysis for computer-based topography and interferometry*, *J. Opt. Soc. Am.* **72** (1982) 156.

[5] H. Suk, N. Barov, J.B. Rosenzweig and E. Esarey, *Plasma electron trapping and acceleration in a plasma wake field using a density transition*, *Phys. Rev. Lett.* **86** (2001) 1011.

[6] M. Kirchen et al., *Optimal Beam Loading in a Laser-Plasma Accelerator*, *Phys. Rev. Lett.* **126** (2021) 174801.

[7] L.T. Ke et al., *Near-GeV Electron Beams at a Few Per-Mille Level from a Laser Wakefield Accelerator via Density-Tailored Plasma*, *Phys. Rev. Lett.* **126** (2021) 214801.

[8] C.J. Tay et al., *A new method for phase extraction from a single fringe pattern*, *Opt. Commun.* **239** (2004) 251.

[9] K. Staszek and M. Bogusz, *Simple fringe pattern normalization algorithm*, *IFAC Proc. Vol.* **45** (2012) 353.

[10] G. Pretzier et al., *Comparison of Different Methods of Abel Inversion Using Computer Simulated and Experimental Side-On Data*, *Z. Naturforsch. A* **47** (1992) 955.

[11] D.D. Hickstein et al., *A direct comparison of high-speed methods for the numerical Abel transform*, *Rev. Sci. Instrum.* **90** (2019) 065115 [arXiv:1902.09007].

[12] M. Born and E. Wolf, *Principles of Optics*, Cambridge University Press (1999) [DOI:10.1017/CBO9781139644181].

2023 JINST 18 C12016